

# Characterization of Silicon Strip Sensors

by

Afaldy Hayeeteh  
afaldy.hayeeteh@gmail.com

and

Md Rounak Jahan Raj  
rounakjahanraj@gmail.com

Submitted to the Department of Physics

in fulfillment of Advanced Laboratory course for the degrees  
of International Master on Advanced methods in Particle Physics

at

**Technische Universität Dortmund**

May 2025

## Abstract

*This report presents a comprehensive characterization of a silicon strip sensor using the Alibava detector system. The study includes measurements of current-voltage characteristics, pedestal and noise behavior, calibration response, charge collection efficiency and large source scan. A reverse bias voltage exceeding the depletion voltage was applied to ensure full sensor depletion. Calibration was performed by injecting known charges and fitting the detector response using a polynomial function. Charge collection efficiency was analyzed using both laser pulses and a  $\beta$  radiation source and the pitch width of the strips was determined using a focused laser scan. A large-source scan revealed the spatial response of the detector. The energy spectrum showed characteristics consistent with a Landau distribution, as expected for thin silicon sensors. These measurements confirm the detector's reliability and suitability for high-precision tracking in high-energy physics experiments.*

# Contents

<b>1</b>	<b>Introduction</b>	<b>1</b>
1.1	The ATLAS Detector . . . . .	1
1.2	Semiconductors . . . . .	2
1.2.1	Doping in Semiconductors . . . . .	2
1.2.2	P-N Junction . . . . .	3
1.3	Energy Spectrum in the Silicon Sensor . . . . .	4
<b>2</b>	<b>Experimental Setup</b>	<b>5</b>
<b>3</b>	<b>Results and Analysis</b>	<b>6</b>
3.1	Current-Voltage Characteristic . . . . .	6
3.2	Pedestals and Noise . . . . .	7
3.3	Calibration Measurements . . . . .	8
3.4	Measurement of Strip Sensor Pitch Width . . . . .	9
3.5	Charge Collection Efficiency . . . . .	10
3.6	Large Source Scan . . . . .	12
<b>4</b>	<b>Conclusion</b>	<b>15</b>

# Chapter 1

## Introduction

The Large Hadron Collider (LHC) at CERN is the largest particle physics research facility which constantly collides hadrons primarily protons and heavy ions to study the tiniest of materials and helps us to understand nature deeply. It mainly consists of four detectors, namely, ALICE, ATLAS, CMS and LHCb.

### 1.1 The ATLAS Detector

The ATLAS detector is a general purpose detector which investigates a wide range of physics including Higgs boson, dark matter candidates and extra dimensions. The schematic diagram of an ATLAS detector is shown below in Figure 1-1:

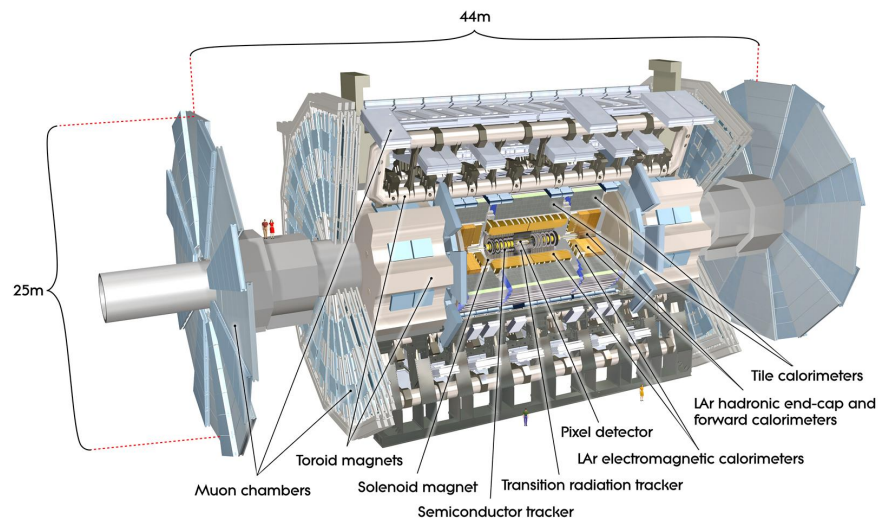


Figure 1-1: Schematic diagram of the ATLAS detector. [1]

The ATLAS detector is built cylindrically around the beam tube. It is constructed in several layers. Directly at the beam tube is the so-called *Inner Detector* (ID), which currently

consists of the *Pixel Detector*, the *Silicon Strip Detector* (SCT3) and the *Transition Radiation Tracker* (TRT). The interactions in the ATLAS detectors create an enormous flow of data. To digest the data, ATLAS uses an advanced “trigger” system to tell the detector which events to record and which to ignore. Complex data-acquisition and computing systems are then used to analyze the collision events recorded. At 46 m long, 25 m high and 25 m wide, the 7000-tonne ATLAS detector is the largest volume particle detector ever constructed. The apparatus in the experiment contains sensor that has 128 individual strips.

## 1.2 Semiconductors

Semiconductor materials are materials whose electrical conductivity is between conductors and insulators having resistances typically in the range  $10^{-6} \Omega\text{m}$  and  $10^{13} \Omega\text{m}$ . Semiconductor materials can be classified into three groups: *element semiconductors* such as germanium, silicon and selenium, *compound semiconductors* such as gallium arsenide and *organic semiconductors*, such as carbon compounds.

The characterization of semiconductors are done based on the band gap which is the energy gap between the valence and conduction band. Typically, the band gap of Silicon is 1.12 eV in room temperature. The band diagram of a *elemental semiconductor* is shown below in Figure 1-2:

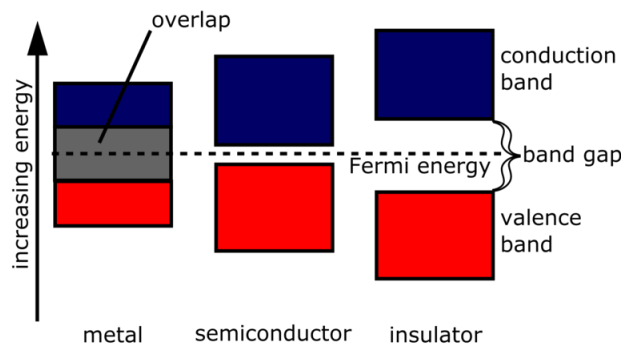


Figure 1-2: Band gaps of conductors (metals), semiconductors and insulators.

### 1.2.1 Doping in Semiconductors

To increase the conductivity of semiconductor material, foreign materials can be doped which increases the charge carrier density. Undoped semiconductors are called intrinsic semiconductors. The Silicon intrinsic semiconductor has a charge density of  $1.5 \times 10^{10} \text{ cm}^{-3}$ . This can be significantly improved by doping. There are two types of doping: p-type doping and n-type doping.

In a n-type doping, a lattice atom of the Silicon crystal is exchanged for a foreign atom that has one electron more in the valence band than silicon. On the contrary, in a p-type semiconductor, the silicon crystal is doped with an element that has fewer than four electrons in the valence shell. In both cases, the current flow is determined by diffusion and drift velocity of the charge carriers. Both types of doping is shown in Figure 1-3:

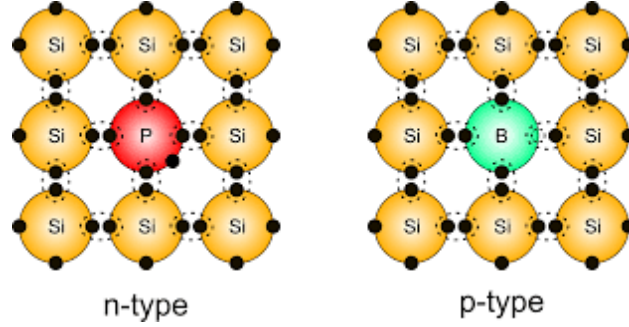


Figure 1-3: n-type and p-type doping for Silicon crystal.

### 1.2.2 P-N Junction

The interface between a p-type and an n-type semiconductor within a single crystal is called p-n junction. It is very crucial for semiconductor detectors such as pixel and strip detector of ATLAS. Initially, in p-n junction, diffusion occurs due to the imbalance of majority charge carriers. Later, equilibrium is established between drift and diffusion currents resulting in a depletion zone.

For the experiment, a negative bias has been used which means negative potential is connected to the p-side and the positive potential is connected to the n-side. This increases the depletion zone. The thickness of the zone depends on the applied voltage. The thickness of the depletion zone can be approximated as:

$$d_c(U) = D \sqrt{\frac{U}{U_{dep}}} \text{ for } U < U_{dep} \quad (1.1)$$

$$d_c(U) = D \text{ for } U \geq U_{dep} \quad (1.2)$$

where,  $U$  is the applied voltage,  $U_{dep}$  is the depletion voltage and  $D$  is the thickness of the sensor.

The energy deposition of an ionizing particle can only be detected to its full extent when the sensor is fully depleted and thus generated electron-hole pairs do not recombine directly. Ideally, no current flows through the semiconductor in this situation, as it has no free charge carriers. In reality, however, thermal excitation leads to the formation of unwanted electron-hole pairs, which are then prevented from recombining by the applied bias voltage in the depletion zone and are conducted to the poles, which is referred to as leakage current.

### 1.3 Energy Spectrum in the Silicon Sensor

In silicon sensors, the energy loss of traversing electrons depends on the sensor thickness. For thick sensors, the energy spectrum tends to follow a Gaussian distribution due to the central limit theorem, as the electron undergoes many interactions. However, in thin sensors like the one used in this experiment (with a thickness of  $300\text{ }\mu\text{m}$ ), there aren't enough interactions to satisfy the central limit theorem. As a result, the energy distribution becomes asymmetric and is better approximated by a Landau distribution. This is because not all secondary electrons are decelerated and absorbed in thin sensors. This leads to variations in the total deposited energy.

Moreover, the electrons from the  $\beta$  source are not mono-energetic, which further affects the shape of the distribution. Therefore, the observed energy spectrum is best described by a convolution of a Gaussian and a Landau distribution. This combined distribution accurately represents the deposited energy in thin silicon sensors. The most probable energy loss, known as the MPV (Most Probable Value), is lower than the mean energy loss in a Landau distribution. This is shown below in Figure 1-4:

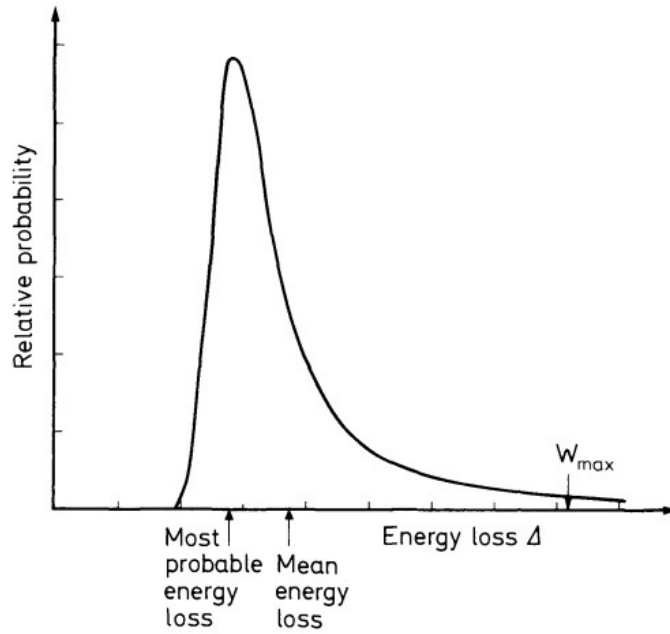


Figure 1-4: Typical distribution of energy loss in a thin absorber.

In practice, the energy deposition is measured in ADC counts, which must be converted into physical energy units like keV. This conversion is done using a polynomial function and takes into account the energy needed to generate electron-hole pairs in silicon (about 3.6 eV per pair). Calibration of the system enables this conversion, allowing the actual deposited energy to be determined.

# Chapter 2

## Experimental Setup

The Alibava EASy is a detector system consisting of three components: the detector unit, the control unit and a computer that controls the data acquisition. The software to control the system is done via the Alibava-gui.

The detector unit consists of the semiconductor sensor and the corresponding readout electronics. The detector unit contains the semiconductor sensor and the corresponding readout electronics. The detector unit includes a silicon sensor with 128 strips and readout electronics. Charge signals from the sensor are sent via wires to a BEETLE chip—also used in LHCb—which amplifies and converts them into voltage signals stored in a pipeline. When triggered, the control unit retrieves the oldest signal, digitizes it, and converts it into ADC counts. If no trigger occurs, the signals are discarded. To measure the signals effectively, the sensor must be depleted and the depletion voltage is usually,  $U_{dep} \approx 60$  to  $80$  V.

The control unit is used to control the detector unit and the bias voltage can be controlled from this unit. Additionally, the Alibava-gui is used to control the Alibava system. Examples of its functionality include starting of the measurement, collecting data for different criteria and saving files effectively.

## Analysis System

During signal generation of the strip sensors, the noise of the strips and the readout electronics is always converted into ADC counts and stored. A signal-to-noise cut is used to distinguish the relevant signal from the noise. This is done by dividing the signal generated by the  $\beta^-$  particle passing through by the noise of the strip. This is compared with the set  $S/N_{textcut}$ . The signal is considered only if it is large enough.

Clusters form when multiple neighboring strips detect a single signal. This can result from charge sharing (when a particle passes near a strip edge), crosstalk (signal interference between strips), or particles passing through the sensor at an angle, affecting several strips.



# Chapter 3

## Results and Analysis

The purpose of this section is to analyze the key characteristics of silicon strip sensors used in high-energy physics by measuring the current-voltage relationship, pedestals and noise behavior, strip pitch width, calibration measurements, and charge collection efficiency.

### 3.1 Current-Voltage Characteristic

The measurement was carried out by increasing the reverse bias voltage in 10 V steps until the current reached a plateau without using a radiation source. However, the process was stopped at 170 V to avoid high voltages that could cause harm to the sensor. The relationship between voltage (V) and current ( $\mu\text{A}$ ) for the sensor is shown in Figure 3-1.

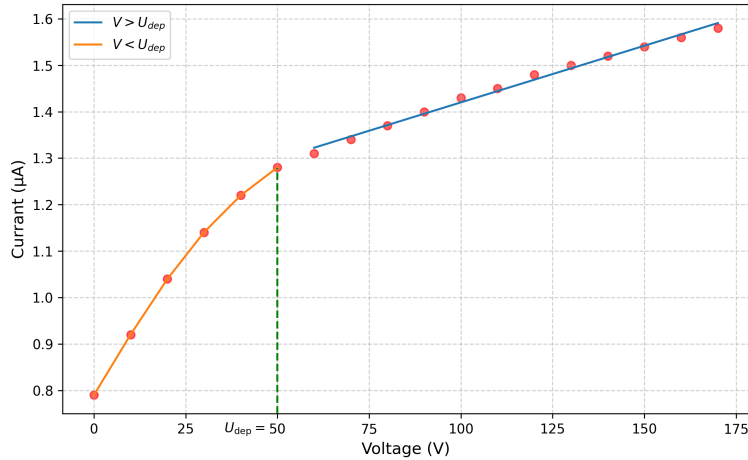


Figure 3-1: Current-voltage curve showing the electrical characteristics of the silicon strip sensor.

The depletion voltage is estimated to be 50 V approximately. The curve reflects the properties of the p-n junction which creates a depletion region where no free charge carriers exist. When a reverse bias is applied, the depletion region expands progressively as expected and can be

divided into two regions: the exponential-like and linear-like regions. Theoretically, once the depletion region extends across the entire p-n junction, the current  $I$  becomes linear.

## 3.2 Pedestals and Noise

To proceed with further experiments, the reverse bias voltage is adjusted to be approximately 20 V higher than the depletion voltage. Without a radiation source, the sensor still produces noise, as shown in Figures 3-2 and 3-3. The signal and noise can be formulated as follows.

$$\text{ADC}(i, k) = P(i) + D(k) + \text{Signal}(i, k) \quad (3.1)$$

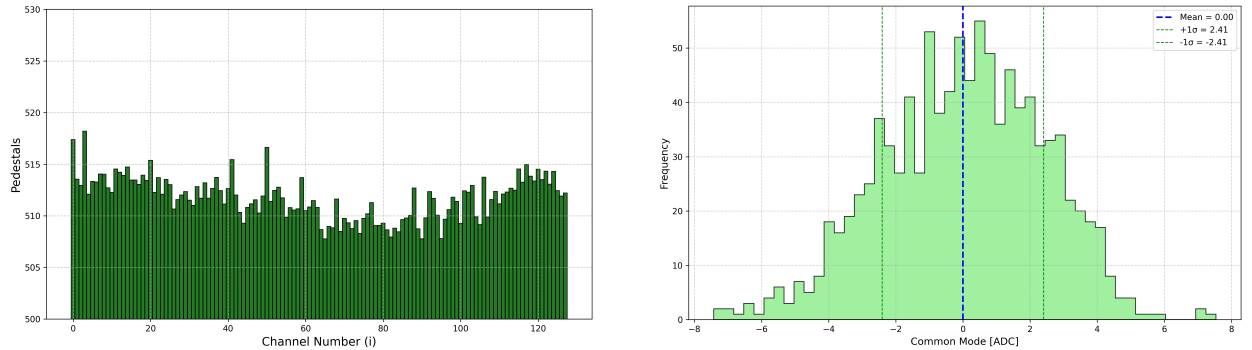
Where the measured  $\text{ADC}(i, k)$  representing signal  $k$  at strip  $i$  is composed of the pedestal  $P(i)$  and the common mode shift  $D(k)$ . Both  $P(i)$  and  $D(k)$  are described by the equations 3.2 and 3.3 respectively.

$$P(i) = \frac{1}{N} \sum_{k=1}^N \text{ADC}(i, k) \quad (3.2)$$

Where  $N$  is the number of events; in this case,  $N = 1000$ . The experimental results for  $P(i)$  are shown in Figure 3-2(a).

$$D(k) = \frac{1}{S} \sum_{i=1}^S (\text{ADC}(i, k) - P(i)) \quad (3.3)$$

Where  $S$  is the number of strips in the detector. For this experiment,  $S = 128$ . Figure 3-2(b) shows the results for  $D(k)$ . The distribution follows a Gaussian distribution, with the mean value around 0, as theoretically expected.



(a) Pedestal  $P(i)$  values for each strip in the detector.

(b) Common mode shift  $D(k)$  distribution in the detector.

Figure 3-2: Two types of noise in the silicon strip detector, Pedestal and Common Mode Shift, as formulated in Equation 3.1.

Therefore, noise can be calculated using Equation 3.4. Ideally, without a source of radiation, the noise term would be zero. However, the result in Figure 3-3 clearly shows that the strip

detector has some dark current caused by thermal excitation.

$$\text{Noise}(i) = \sqrt{\frac{1}{N-1} \sum_k^N (\text{ADC}(i, k) - P(i) - D(k))^2} \quad (3.4)$$

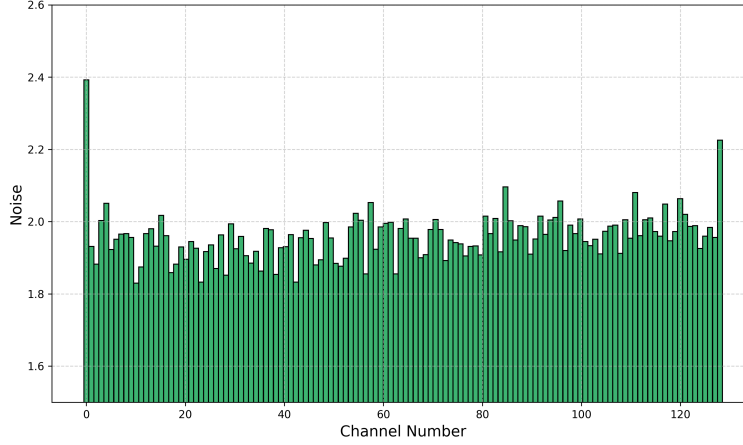


Figure 3-3: Noise values in each strip channel, showing evidence of thermal excitation affecting the dark current in the detector.

The first strip and the last one show exceptionally high noise values. This can be interpreted as follows: inner strips are shielded by neighboring strips, reducing external interference while edge strips are exposed on one side making them pickup noise or cross-talk from nearby electronics.

### 3.3 Calibration Measurements

A Silicon strip detector is designed to produce electrical signals when energy from radiation or incident particles is deposited into the strips. To calibrate the detector, this experiment was conducted by injecting pulses into the readout ASIC (BEETLE). The configuration for the calibration measurement is: number of pulses = 256 and charge ( $e^-$ ) = 260,000.

The scatter plot in Figure 3-4 shows the relationship between ADC and the energy injected into the detector. At low energies, ADC counts increase linearly with energy deposited, but at high energies, nonlinear effects cause the ADC response to grow faster than linearly, similar as an exponential increase. The pattern curve clearly shows the limitation of signal generation for this type of detector. To obtain the deposited energy from the ADC value, a 4th-degree polynomial function  $f(x) = a + bx + cx^2 + dx^3 + ex^4$  is applied to fit Figure 3-4. A summary of the coefficients in the fitting function is provided in Table 3.1.

Table 3.1: Coefficients for the 4th-degree polynomial function

Coefficient	Value
$a$	$1.01 \times 10^{-2}$
$b$	$2.74 \times 10^{-4}$
$c$	$1.60 \times 10^{-5}$
$d$	$-1.10 \times 10^{-7}$
$e$	$2.77 \times 10^{-10}$

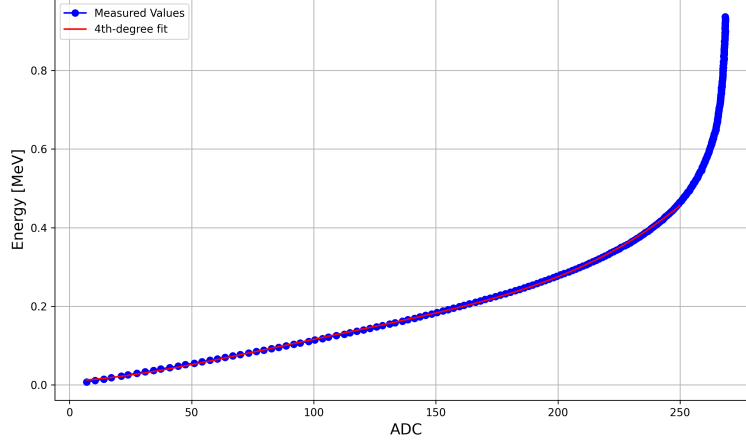
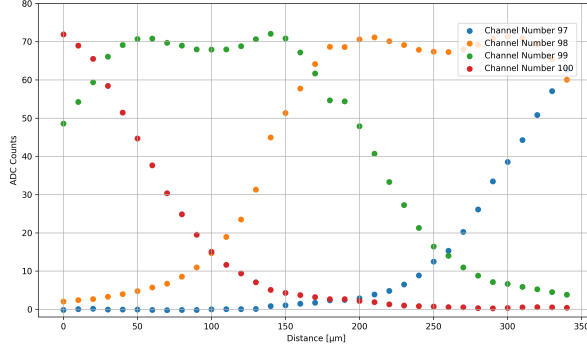


Figure 3-4: Calibration curve showing the detector response (ADC counts) as a function of the injected energy.

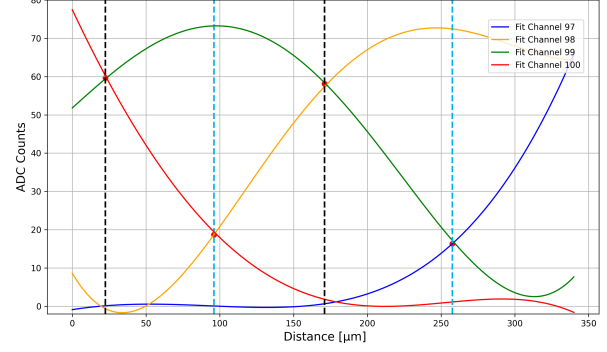
### 3.4 Measurement of Strip Sensor Pitch Width

In high-energy physics, the resolution of a detector significantly affects the results. For that reason, the strip sensor structure needs to be investigated. In this experiment, the detector is injected with a laser pulse, starting by measuring the optimal delay between the laser signal and the chip readout. Then, measurements are taken at  $10\text{ }\mu\text{m}$  intervals from the optimal point for a total of 35 steps.

Since the laser is applied to a specific range of detector, Figure 3-9 shows that only channels 97, 98, 99, and 100 exhibit high signal intensity. The behavior shown in the Figure (a) shows the expected oscillating pattern where a strip produces a high ADC signal when facing the laser and gradually decreases as the laser moves away. In this case, channel number 100 starts with the highest ADC signal, which slowly decreases as it moves to channel number 99. Then, channel 99's signal becomes the highest, and the same pattern continues as the signal moves to channels 98 and 97.



(a) ADC signals as a function of the distance



(b) Fitted curve of ADC signal as a function of the distance

Figure 3-5: Plots of ADC versus distance from the first optimal point to 350  $\mu\text{m}$  from the optimal point for strip channel numbers 97, 98, 99, and 100.

To determine the strip sensor pitch width, the intersections between the periodic patterns must be identified. By fitting the Figure, the intersection points can be effectively identified as shown by the red points in Figure 3-9(b). In this experiment, the pitch width can be calculated as the difference between the intersection points. The first width corresponds to the distance between channels 100 and 99, and the second corresponds to the distance between channels 98 and 97. The pitch widths are summarized in the table 3.2.

Table 3.2: Pitch widths of the sensor.

Channel numbers	Pitch width [ $\mu\text{m}$ ]
97–98	148.54
99–100	161.48
Mean	155.01

### 3.5 Charge Collection Efficiency

The efficiency of a strip detector is measured by how effectively the device collects electrons and holes generated by incident radiation before they recombine as described by formula 3.5. It is usually expressed as a percentage or a fraction between 0 and 1.

$$\text{CCE} = \frac{\text{Collected charge}}{\text{Generated charge}} \quad (3.5)$$

Figure 3-6(a) shows a similar pattern for both the laser pulse and the radiation source. As the reverse bias voltage increases, the CCE approaches a plateau. The initial of this plateau occurs at the depletion voltage of 85V, where the CCE is approximately above 0.9. Another clear distinction between the laser and the radiation source is that the CCE rises more quickly for the laser. This is because the laser does not go very deep into the detector and generates electron-hole pairs closer to the surface, making them easier to collect. In contrast,

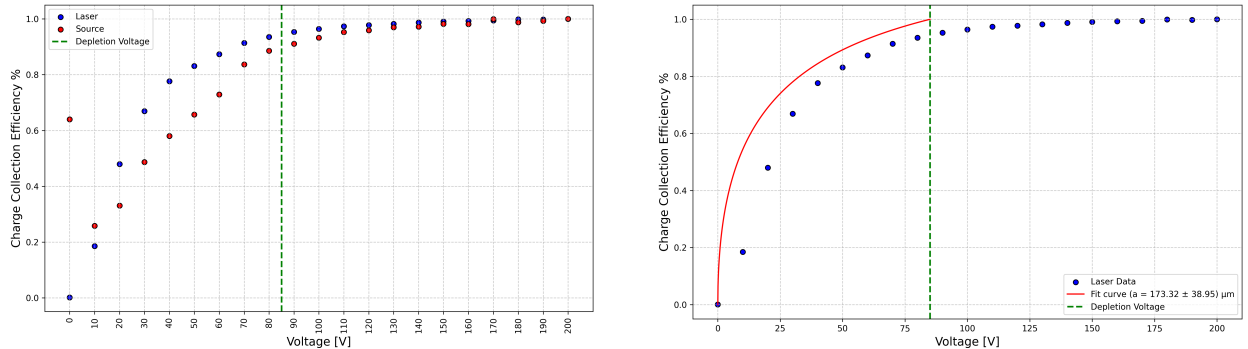
the radiation source creates electron-hole pairs throughout the detector volume. Thus, the source need more reverse bias voltage to be fully collected.

To compare with the theoretical prediction, the CCE curve can be calculated using equation 3.6. In the equation,  $D = 300$  micrometers represents the thickness of the detector,  $V$  is the reverse bias voltage,  $U_{\text{dep}}$  is the depletion voltage, and  $a$  is the penetration depth of the laser into silicon.

$$\text{CCE} = \frac{1 - \exp\left(-\frac{D\sqrt{\frac{V}{U_{\text{dep}}}}}{a}\right)}{1 - \exp\left(-\frac{D}{a}\right)} \quad (3.6)$$

The property of the laser can be characterized by the penetration depth  $a$ , which represents how far the laser penetrates into the silicon. As having done so far, Figure 3-6(b) shows the predicted curve based on the equation and provides the value of  $a = 173.32 \pm 40.00 \mu\text{m}$

The fitting result does not accurately reflect the trend observed in the graph. This discrepancy may be due to an experimental error, where the actual depletion voltage is 50 V based on the analysis in Figure 3-1, but it was misidentified as 85 V during the experiment. This misreading of the voltage is reflected in the fitting result.



(a) CCE percentage versus reverse bias voltage measured using a radiation source and laser pulse.

(b) Fitted prediction curve based on the equation 3.6 versus reverse bias voltage

Figure 3-6: The CCE percentage as a function of the reverse bias voltage along with the fitted curve based on theoretical prediction.

The fit in Figure 3-6b looks quite poor, probably because the cut that had been used in the fitting is not the same as the depletion voltage 50 V which is much lower than the cut. Moreover, in Figure 3-6a the laser is rising more quickly compared to the source. The reason for this is probably that the laser is not penetrating the whole detector and creates the electron-hole pairs closer to the surface which makes it easier to absorb them, while the source is creating electron-hole pairs all along the way.

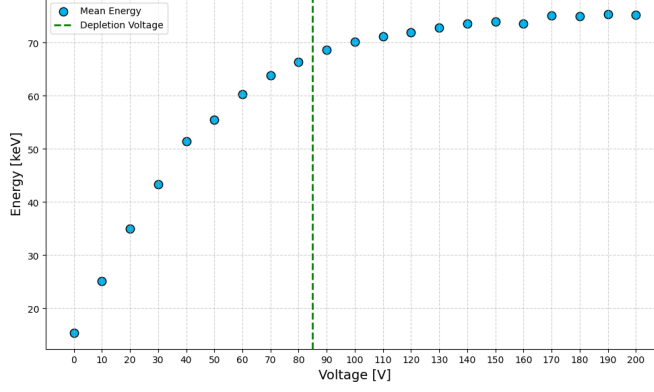


Figure 3-7: The mean cluster energy plotted versus the reverse bias voltage.

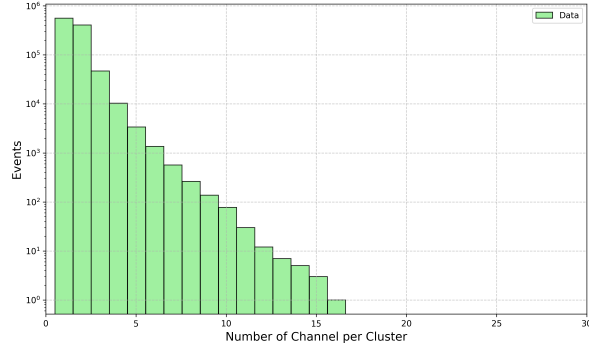
To better relate to a physical observable, Figure 3-7 shows the the mean cluster energy calibrated from Section 3.4 plotted against the reverse bias voltage. The maximum of mean deposited energy is approximately 75.41 keV, which is consistent with the MPV value in the next section around 90 keV for the large source scan in Figure 3-10. This figure shows a pattern similar to the CCE graph that a gradual increase in energy and then followed by a plateau at the maximum value. This pattern indicates that the reverse bias voltage expands the depletion region of the p-n junction until it covers the entire silicon. The most probable values of the deposited energy contributes to determining the resolution of the detector.

### 3.6 Large Source Scan

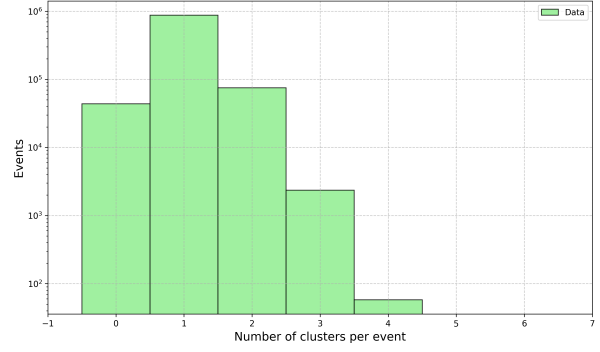
In the last measurement, the strip detector was exposed to a radioactive source 1,000,000 runs moved across it to evaluate the response uniformity, identify dead or noisy strips, and map its response.

As shown in Figure 3-8, in histogram (a), the number of strips registering the same signal decreases linearly up to 16 strips per cluster. This means the charge mostly spreads to a small number of strips which is expected in a well-functioning Silicon strip detector.

Moreover, histogram (b) shows the number of clusters per event, with a concentration around 0, 1, 2, and 3 clusters. The 0th bar represents events where only a single strip was hit indicating no cluster formation. In contrast, the 1st, 2nd, and 3rd bars correspond to events with one, two, and three clusters, respectively. The concentration at low cluster numbers suggests that the detector is not overwhelmed by noise or false signals.



(a) Distribution of the number of strips per cluster.



(b) Distribution of the number of clusters per event.

Figure 3-8: In a strip silicon detector, a cluster is a group of adjacent strips that register a signal from the same particle passing through. This figures shows the detector's behavior based on the number of clusters registered in the strips and each event.

To investigate further, the spectrum of the number of events detected by each strip channel is shown in Figure 3-9. The shape of the distribution can be interpreted as this measurement setup placed the source directly near strip number approximately 80 since it clearly shows symmetry at strip numbers 32 and 128. This indicates the detector is working properly as expected where detecting more events where the source is closest.

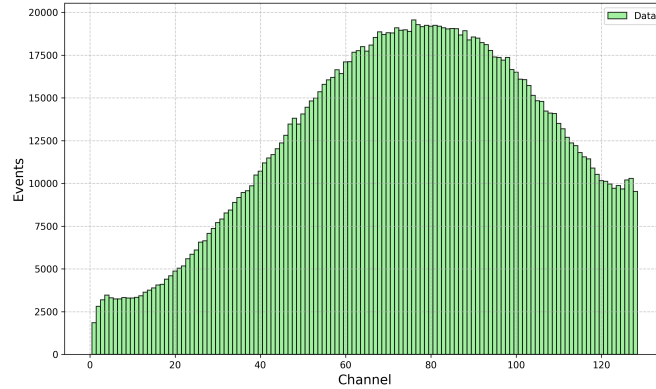
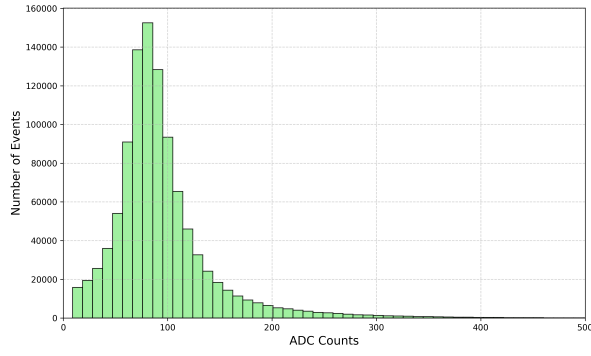


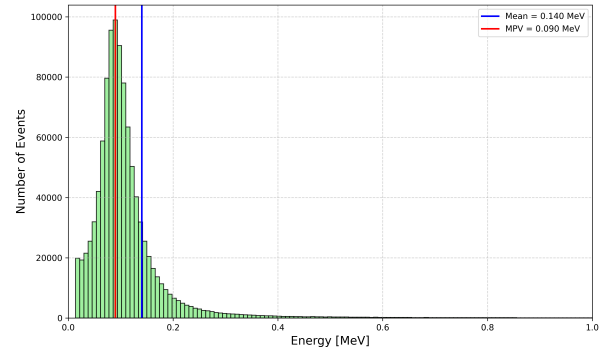
Figure 3-9: Distribution of the number of events by the different strip channel.

The final measurement is to investigate the shape of the energy spectrum in the silicon sensor. For better understanding, the data have been calibrated as described in section 3-4. Figure 3-10 shows both the experimental data and the calibrated data. The mean and most probable values of the deposited energy are about 140 keV and 90 keV respectively, indicating a key characteristic of the Landau distribution from theory 1-4.





(a) Energy spectrum represented in ADC counts



(b) Energy spectrum represented in MeV

Figure 3-10: Energy spectrum in the Silicon sensor: raw data and calibrated data.

# Chapter 4

## Conclusion

The silicon strip sensor was successfully characterized through a series of experimental measurements. The current-voltage curve allowed for the estimation of the depletion voltage, which was found to be approximately 85 V. To ensure full depletion and stable performance, the sensor was operated at 105 V during subsequent measurements. Pedestal and noise analysis revealed thermal contributions in the absence of a radiation source, while calibration measurements established a nonlinear response between the injected charge and ADC output. The pitch width between the sensor strips was determined with high precision through laser scanning, yielding an average value of about 155  $\mu\text{m}$ . Charge collection efficiency measurements demonstrated the sensor's full efficiency at voltages above the depletion threshold, consistent with theoretical predictions. Finally, the energy deposition spectrum showed a shape characteristic of a Landau distribution, confirming the expected behavior for thin silicon sensors. Overall, the detector exhibited reliable and accurate performance, confirming its effectiveness for tracking applications in particle physics experiments especially inside the ATLAS detector.

# Literatures

- [1] Joao Pequena. Computer generated image of the whole ATLAS detector. 2008.